Phase contrast laminography based on Talbot interferometry

Venera Altapova,[1,2,*] **Lukas Helfen,**[3,4] **Anton Myagotin,**[3,5]
Daniel Hänschke,[1] **Julian Moosmann,**[1] **Jan Gunneweg,**[6] **and**
Tilo Baumbach[1,3]

[1]*Laboratorium für Applikationen der Synchrotronstrahlung (LAS), Faculty of Physics, Karlsruher Institut für Technologie (KIT), Postfach 6980, D-76128 Karlsruhe, Germany*
[2]*National Research Tomsk Polytechnic University, Lenina av. 30 Tomsk, Russia*
[3]*ANKA, Institut für Synchrotronstrahlung (ISS) Karlsruher Institut für Technologie (KIT), Hermann-von-Helmholtz-Platz 1, D-76344 Eggenstein-Leopoldshafen, Germany*
[4]*European Synchrotron Radiation Facility, BP-220, F-38043 Grenoble, France*
[5]*Saint-Petersburg State University of Civil Aviation, Pilotov street 38, 196210 Saint-Petersburg, Russia*
[6]*Archaeometry, Institute of Archaeology, The Hebrew University of Jerusalem, Mount Scopus 91905 Jerusalem, Israel*
*venera.altapova@kit.edu

Abstract: Synchrotron laminography is combined with Talbot grating interferometry to address weakly absorbing specimens. Integrating both methods into one set-up provides a powerful x-ray diagnostical technique for multiple contrast screening of macroscopically large flat specimen and a subsequent non-destructive three-dimensional (3-D) inspection of regions of interest. The technique simultaneously yields the reconstruction of the 3-D absorption, phase, and the so-called dark-field contrast maps. We report on the theoretical and instrumental implementation of of this novel technique. Its broad application potential is exemplarily demonstrated for the field of cultural heritage, namely study of the historical Dead Sea parchment.

© 2012 Optical Society of America

References and links

1. Z. des Plantes, "Eine neue Methode zur Differenzierung in der Rontgenographie," Acta Radio. **13**, 182–192 (1932).
2. L. Helfen, A. Myagotin, P. Pernot, M. DiMichiel, P. Mikulík, A. Berthold, and T. Baumbach, "Investigation of hybrid pixel detector arrays by synchrotron-radiation imaging," Nucl. Inst. Meth. A **563**, 163–166 (2006).
3. J. Dik, K. Krug, L. Porra, P. Coan, G. Tauber, A. Wallert, A. Coerdt, A. Bravin, M. Elyyan, L. Helfen, and T. Baumbach, "Relics in medieval altarpieces? combining x-ray tomographic, laminographic and phase-contrast imaging to visualize thin organic objects in paintings," J. Synchrotron Rad. **563**, 163–166 (2007).
4. A. Houssaye, F. Xu, L. Helfen, C. De Buffrénil, T. Baumbach, and P. Tafforeau, "Three-dimensional pelvis and limb anatomy of the Cenomanian hind-limbed snake Eupodophis descouensi (Squamata, Ophidia) revealed by synchrotron-radiation computed laminography," J. Vert. Paleontol. **31**, 2–6 (2011).
5. S. Harasse, N. Hirayama, W. Yashiro, and A. Momose, "X-ray phase laminography with Talbot interferometer," Proc. SPIE **7804**, 780411 (2010).
6. L. Helfen, T. Baumbach, P. Cloetens, and J. Baruchel, "Phase-contrast and holographic computed laminography," Appl. Phys. Lett. **94**(10), 104103 (2009).
7. M. Hoshino, K. Uesugi, A. Takeuchi, Y. Suzuki, and N. Yagi, "Development of x-ray laminography under an x-ray microscopic condition," Rev. Sci. Instrum. **82**, 073706 (2011).

8. G. Schulz, T. Weitkamp, I. Zanette, F. Pfeiffer, F. Beckmann, C. David, S. Rutishauser, E. Reznikova, and B. Müller, "High-resolution tomographic imaging of a human cerebellum: comparison of absorption and grating-based phase contrast," J. Roy. Soc. Interf. **7**, 1665–1676 (2010).

9. T. Weitkamp, C. David, O. Bunk, J. Bruder, P. Cloetens, and F. Pfeiffer, "X-ray phase radiography and tomography of soft tissue using grating interferometry," Eur. J. Radiol. **68S**, 13–17 (2008).

10. L. Helfen, T. Baumbach, P. Mikulík, D. Kiel, P. Pernot, P. Cloetens, and J. Baruchel, "High-resolution three-dimensional imaging of flat objects by synchrotron-radiation computed laminography," Appl. Phys. Lett. **86**, 071915 (2005).

11. L. Helfen, A. Myagotin, P. Mikulík, P. Pernot, A. Voropaev, M. Elyyan, M. Di Michiel, J. Baruchel, and T. Baumbach, "On the implementation of computed laminography using synchrotron radiation," Rev. Sci. Instrum. **82**, 063702 (2011).

12. T. Weitkamp, A. Diaz, C. David, F. Pfeiffer, M. Stampanoni, P. Cloetens, and E. Ziegler, "X-ray phase imaging with a grating interferometer," Opt. Express **13**, 6269–6304 (2005).

13. F. Pfeiffer, C. Kottler, O. Bunk, and C. David, "Phase retrieval and differential phase-contrast images using polychromatic hard X-rays," Nat. Phys. **2**, 258–261 (2006).

14. A. Momose, W. Yashiroi, and Y. Takeda, "X-ray phase imaging with Talbot interferometry," in *Biomedical Mathematics:Promising Directions in Imaging, Therapy Planning, and Inverse Problems,* Y. Censor, M. Jiang, and G. Wang, eds. (Medical Physics Publishing, 2010), pp. 281–320.

15. F. Natterer, *The Mathematics of Computerized Tomography* (Society for Industrial and Applied Mathematics, 2001).

16. P. Mikulík, and T. Baumbach, "X-ray reflection by rough multilayer gratings: dynamical and kinematical scattering," Phys. Rev. B **59**, 7632–7643 (1999).

17. F. Pfeiffer, M. Bech, O. Bunk, P. Kraft, E.F. Eikenberry, C. Brönniman, C.Grünzweig, and C. David, "Hard-X-ray dark-field imaging using a grating interferometer," Nat. Mater. **7**, 134–137 (2008).

18. F. Xu, L. Helfen, T. Baumbach, and H. Suhonen, "Comparison and quantification of laminography and limited-angle-tomography," Opt. Express , submitted (2011).

19. A. Myagotin, A. Voropaev, L. Helfen, D. Hänschke, and T. Baumbach, "Fast volume reconstruction for parallel-beam computed laminography by filtered backprojection," J. Parallel Distrib. Comput., submitted (2011).

20. F. Pfeiffer, C. Kottler, O. Bunk, and C. David, "Hard x-ray phase tomography with low-brilliance sources," Phys. Rev. Lett. **98**, 108105 (2007).

21. I. Zanette, T. Weitkamp, T. Donath, S. Rutishauser, and C. David, "Two-dimensional x-ray grating interferometer," Phys. Rev. Lett. **105**, 248102 (2010).

22. D. Bradley and D. Creagh, *Physical techniques in the Study of Art, Archaeology and Cultural Heritage* (Elsevier, 2007).

23. R. Larsen, *Microanalysis of Parchment* (Archetype Books, 2007).

24. B.M. Murphy, M. Cotte, M. Mueller, M. Balla and J. Gunneweg, "Degradation of parchment and ink of the Dead Sea scrolls investigated using synchrotron-based X-ray and infrared microscopy, in Holistic Qumran," in *Holistic Qumran,* J. Gunneweg, A. Adriaens and J. Dik, eds. (Brill Leiden, 2010), pp. 77–98.

25. J. Dik, L. Helfen, P. Reischig, J. Blaas, and J. Gunneweg, "A short note on the application of synchrotron-based micro-tomography on the Dead Sea scrolls in Holistic Qumran," in *Holistic Qumran,* J. Gunneweg, A. Adriaens and J. Dik, eds. (Brill Leiden, 2010), pp. 21–28.

1. Introduction

Modern x-ray imaging methods are among the most important physical measuring tools of clinical diagnostics, non-destructive testing as well as imaging diagnostics in fundamental research. Already in the thirties of the last century, early laminography concepts enabled to obtain (yet blurred) 2-D slices of internal structures in laterally extended 3-D objects [1].

The tremendous ongoing progress in computation technology, mathematical algorithms and fast 1-D and 2-D detector technology led to 2-D and 3-D computed tomography (CT) and computed laminography (CL) techniques with manifold applications in medical and industrial imaging as well as homeland security. The implementation of 3-D tomographic and laminographic techniques at modern synchrotron facilities increased further spatial and temporal resolution, thanks to the strongly enhanced flux at synchrotron sources compared to conventional x-ray tubes.

An increase of spatial resolution for a fixed number of pixels goes together with a decreasing field of view of the detector. This circumstance increasingly restricts the maximum lateral dimensions of the specimen to be probed by tomography, at least under optimal experimental

conditions. That is, if the x-ray beam path captures a constant sample volume, which is sufficiently penetrated by the beam. Under such advantageous conditions, 3-D tomography permits the most complete sampling of the specimen's Fourier space (reciprocal space).

As favorable illumination and penetration conditions can be maintained only for objects with dimensions below the detector's effective field of view, for larger samples one has to accept compromises, for example to trim the specimen to fit the field of view by sample dissection, or by applying modified scanning schemes. Synchrotron radiation computed laminography (SRCL) represents such a modified scanning scheme which allows examining, without sample cutting, a class of specimen where *lateral* dimensions strongly exceed the effective field of view (like rather flat specimens such as electronic circuit boards).

SRCL provides a possibility to zoom into regions of interest of macroscopically large specimen with microscopic resolution without touching their integrity. The method has extended the scientific application range of 3-D synchrotron imaging to such samples in engineering sciences, paleontology and cultural heritage [2–4]. Similar to tomography, applications of SRCL can be further broadend by their combination with phase contrast imaging methods and/or microscopy techniques [5–7].

In the present paper, we report on the realization of multiple contrast laminography imaging based on Talbot grating interferometry. Among existing phase contrast imaging methods, Talbot grating interferometry (TGI) offers high phase sensitivity and can be utilized even with low-resolution detectors and laboratory x-ray sources. In combination with computed tomography, phase contrast imaging with a grating interferometer has produced remarkable results in imaging soft tissue, such as brain, heart, and uretra (see e.g. [8,9]).

By implementation of TGI into a dedicated laminography set-up we intend to bring together the advantages of both methods. The paper is organised as follows: we first outline the methodical principles and the theoretical approach of the 3-D imaging method. Then we briefly describe our instrumental implementation. Finally, we apply the method exemplarily for x-ray diagnostics of fresh parchment and historical one from the so-called Dead Sea scrolls.

2. Principles of Talbot grating interferometry based laminography

Fundamental methodical principles and theoretical treatments of SRCL and of TGI as individual techniques have been described in a series of papers, see for example [10–13], and [14] for comprehensive theoretical descriptions of TGI. This section summarizes and merges above treatments into a compact theoretical description of 3-D TGI-based computed laminography.

Image acquisition via grating-based computed laminography contains four steps: (1) tilting of the rotation axis from the ordinary tomographic axis relatively to the optical beam path by the laminography tilt angle θ, (2) radiography of the grating interferometry image sequences (phase-stepping technique), (3) recording the laminographic φ rotation scans, if required, also in a loop together with (4) transversal (x, y) sample screening.

In the following we define by $\mathscr{F}_n^{-1}, \mathscr{F}_n$ for forward and backward n-dimensional Fourier transforms. The real space vectors $\mathbf{r}$ are written in the laboratory coordinate system as $\mathbf{r} = u\mathbf{e}_u + v\mathbf{e}_v + w\mathbf{e}_w$ and in the specimen coordinate system as $\mathbf{r} = x\mathbf{e}_x + y\mathbf{e}_y + z\mathbf{e}_z$. For convenience we place the origin of both coordinate systems in the rotation centre of the laminography set-up. A similar notation is used for reciprocal (Fourier) space vectors, writing, e.g., wave vectors in the laboratory system as $\mathbf{K} = K_u\hat{\mathbf{e}}_u + K_v\hat{\mathbf{e}}_v + K_w\hat{\mathbf{e}}_w$. Further, we define w being the optical axis and u and v the horizontal and vertical axes of the rectangular image plane with $\mathbf{r}_\parallel$ or $\mathbf{K}_\parallel$ the projections of $\mathbf{r}$ and $\mathbf{K}$ onto the image planes. The z axis is the laminographic rotation axis, the (x, y) plane is parallel to the laminographic rotation table. In laminography, the specimen's spatial orientation is unambiguously defined by the laminographic rotation and tilt angles φ and θ, see Fig. 1. The laboratory system coordinates are transformed into the specimen coordinate
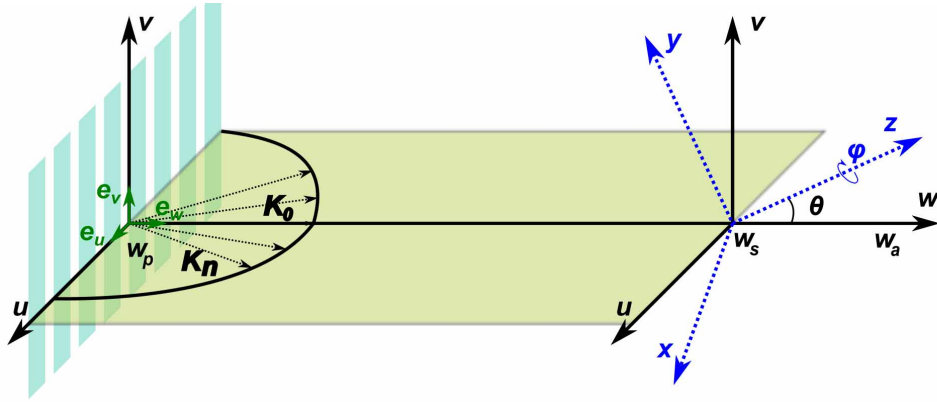
Fig. 1. Propagation geometry and coordinate systems for TGI-based laminography: $\{x, y, z\}$ correspond to the specimen's fixed-body coordinate system, $\{u, v, w\}$ to the laboratory co-ordinate system with the corresponding unit vectors. The laminography tilt angle θ is measured between the rotation axis and the optical axis. φ is the laminographic rotation angle. $\mathbf{K}_0$ is the wave vector of the incident x-ray fronts. The cross section of the Ewald sphere and the grating rods define the wave vectors of the grating diffraction orders $\mathbf{K}_n$.

system according to

$$(x, y, z) = R_z(-\varphi) \cdot R_x(-\theta) \cdot \begin{pmatrix} u \\ v \\ w \end{pmatrix}, \qquad (1)$$

where R_z, R_x are conventional 3×3 matrices describing rotation about the $\mathbf{z}$ and $\mathbf{x}$ axes. The same relation holds for coordinates of all reciprocal space vectors.

Forward problem

The response of matter to x-rays may be well described by the complex refraction index, $n(\mathbf{r}) = 1 - \tilde{\delta}(\mathbf{r}) + i\tilde{\beta}(\mathbf{r})$, which considers refraction by $\tilde{\delta}(\mathbf{r})$ and absorption by $\tilde{\beta}(\mathbf{r})$. Propagation of a plane wave through a grating laminography set-up involves mainly the subsequent interactions of: (a) transmission through the phase grating and diffraction during propagation, (b) transmission through the specimen in dependence on the laminographic angles θ and φ, by which the initially otherwise unperturbed grating diffracted wave field acquires space-dependent disturbances due to refraction, absorption, and scattering by the sample structure, (c) propagation of the perturbed wave field to the image plane (where an absorption grating is positioned), (d) transmission of the corresponding intensity field through the absorption grating. The latter generates a Moiré fringe pattern in the detector plane. Points (a) and (b) can be interchanged.

Theoretical approaches of TGI are based on strong diffraction contributions by the phase grating and treat the specimen as a small pertubation to the diffracted wave field, neglecting any diffraction within the specimen.

The forward problem may start from a sufficiently coherent incident wave field. Let us assume an incident plane wave $\exp(i\mathbf{K}_0\mathbf{r})$ with the wave vector $\mathbf{K}_0$ parallel to the optical axis w. Passing through an object, it undergoes phase and amplitude changes, which in the eikonal or projection approximation are considered by line integrals $p = \int_L \{\mathbf{K} - \mathbf{K}n(\mathbf{r})\}\, dl$. In the object exit plane the transmitted wave field can be written as a perturbed plane wave with inhomoge-

neous amplitude

$$E_T(\mathbf{r}) = \exp\left(-ip_{\varphi,\theta}\left(\mathbf{r}_\parallel\right)\right)\exp\left(iK_0 w\right). \tag{2}$$

Here we have introduced the so-called *x-ray transform* [15], which in the laminographic case is the *complex* 2D disturbance function determined by the three-dimensional integration

$$p_{\varphi,\theta}(\mathbf{r}_\parallel) = p'_{\varphi,\theta}(\mathbf{r}_\parallel) - ip''_{\varphi,\theta}(\mathbf{r}_\parallel) = K\int_{\mathbb{U}^3}\left\{\tilde{\delta}(\mathbf{r}) - i\tilde{\beta}(\mathbf{r})\right\}\delta(\mathbf{r}\mathbf{e}_u - u)\delta(\mathbf{r}\mathbf{e}_v - v)\,d\mathbf{r}. \tag{3}$$

The Dirac delta functions in Eq. (3) select all allowed $\mathbf{r}$, contributing to the projection onto an image plane at point $\mathbf{r}_\parallel = u\mathbf{e}_u + v\mathbf{e}_v$, where $(u\mathbf{e}_u, v\mathbf{e}_v)$ span the rectangular 2-D projection plane.

The integration range comprises the part $\mathbb{U}^3 \in \mathbb{R}^3$ of the three-dimensional space filled by the object corresponding to the x-ray transform (in our case the gratings or the specimen). Although at synchrotron sources the condition of parallel-beam geometry holds very well, the laminography geometry, in contrast to 3-D tomography, does *not* allow for a split of the aquisition and reconstruction problem into a stack of 2-D problems. By use of Eq. (1) the x-ray transforms of the gratings and of the specimen may be alternatively expressed in the laboratory or specimen coordinate system, whereby only the x-ray transform of the specimen explicitly depends on the laminographic tilt and rotation angles.

The x-ray transform of a 1-D or 2-D transmission grating is periodic, the unperturbed diffracted wave field downstream of a grating inherits these symmetry properties and thus can be written as a following expansion into a Fourier series [16]

$$E_G(\mathbf{r}) = \sum_m T_m \exp\left(i\mathbf{K}_m\mathbf{r}\right), \tag{4}$$

with amplitudes T_m and wave vectors $\mathbf{K}_m$. Coefficients T_m can be calculated from Eq. (2) by use of the x-ray transform Eq. (3) of the grating. The allowed wave vectors $\mathbf{K}_m$ are selected by the intersection of the Ewald sphere with so-called grating truncation rods, which represent the grating response function $n_G(\mathbf{r})$ in the Fourier domain, $\mathscr{F}_3(n_G(\mathbf{r}))$, yielding (for gratings aligned in the (u,v) plane) in the paraxial approximation

$$\mathbf{K}_m = \mathbf{h}_m + \left\{K - h_m^2/2K\right\}\hat{\mathbf{e}}_w. \tag{5}$$

The $\mathbf{h}_m$ are reciprocal grating vectors, which are defined by the symmetry and period lengths of the grating (for 1-D gratings, e.g., with periods D along $\mathbf{u}$ it is $\mathbf{h}_m = 2m\pi/D\hat{\mathbf{e}}_u$).

The grating diffraction field becomes perturbed by the specimen disturbance $p_{\varphi,\theta}(\mathbf{r}_\parallel)$ in dependence on the laminographic angles. Within a sufficiently good approximation for TGI, the specimen's x-ray transform $p_{\varphi,\theta}(\mathbf{r}_\parallel)$ *diffractionless* propagates into the bundle of directions $\mathbf{K}_m$ of the plane-wave grating diffraction orders. Diffractionless propagation leads to a geometrical projection. Due to the geometric intercept theorem, a non-zero angle between the $\mathbf{K}_m$ and the optical axis with increasing propagation distances Δw causes an increasing lateral shift $\Delta\mathbf{r}_\parallel = \Delta w\left[\mathbf{K}_{\parallel m}/K\right]$ in the x-ray transform projected along $\mathbf{K}_m$ onto the image plane. The total perturbed wave field in the image plane at the position of the absorption grating w_a consists of the superposition of field contributions of all perturbed grating diffraction orders, obtained by use of the Eq. (2)–(5):

$$E_P(\mathbf{r}_\parallel, w_a) = \sum_m T_m \exp\left(i(\mathbf{r}_\parallel\mathbf{h}_m - w'\,h_m^2/2K)\right)\exp\left(-ip_{\varphi,\theta}(\mathbf{r}_\parallel + \tilde{w}\left[\mathbf{h}_m/K\right])\right). \tag{6}$$

Here $w' = w_a - w_p$ is the axial propagation distance between phase and absorption grating, and $\tilde{w} = w_a - \max(w_s, w_p)$ denotes the axial propagation distance of the specimen disturbance with the grating diffraction field. Every summand in Eq. (6) comprises the contribution of the

unperturbed grating diffraction order (first two factors), which are multiplied with a disturbance factor having the specimen's propagated x-ray transform in its exponent.

In linear approximation of $p_{\varphi,\theta}(\mathbf{r}_\parallel)$ Eq. (6) can be rewritten in the form

$$E_P(\mathbf{r}_\parallel, w_a) = \exp\left(-ip_{\varphi,\theta}(\mathbf{r}_\parallel)\right) \sum_m T_m \exp\left(-iw' \, h_m^2/2K\right) \exp\left(i\mathbf{h}_m \left\{\mathbf{r}_\parallel - \tilde{w}/K\nabla_\parallel p_{\varphi,\theta}(\mathbf{r}_\parallel)\right\}\right). \quad (7)$$

The sensitivity of a certain grating order with respect to the specimen is proportional to the scalar product of the reciprocal grating vector $\mathbf{h}_m$ with the local 2-D gradient vector of the specimen's x-ray transform $\nabla_\parallel p_{\varphi,\theta}$, and it is linearly magnified by the propagation distance $\tilde{w}$. Using the self-imaging properties of unperturbed grating-diffracted fields, the image plane will favorably be positioned at such suitable fractional Talbot orders, where propagation of the initially *phase* modulated wave field of the first grating has developed strong *amplitude* modulation, and as a consequence essential intensity modulation. The unperturbed intensity field of the grating can be expanded in to a Fourier series, $I_G(\mathbf{r}) = \sum_n I_n \exp(i\mathbf{h}_n\mathbf{r})$, and after incorporating the sample, the perturbed intensity pattern can be approximated by

$$I_P(\mathbf{r}) = \exp\left(-2p''_{\varphi,\theta}(\mathbf{r}_\parallel)\right) \sum_n I_n \exp(i\mathbf{h}_n\tilde{\mathbf{r}}) \quad (8)$$

with $\tilde{\mathbf{r}} = \mathbf{r}_\parallel + \Delta\tilde{\mathbf{r}}_\parallel$, and where $\Delta\tilde{\mathbf{r}}_\parallel = \tilde{w}/K \, \nabla_\parallel p'_{\varphi,\theta}(\mathbf{r}_\parallel)$. Here, we assumed that the effect of $\nabla_\parallel p''_{\varphi,\theta}(\mathbf{r}_\parallel)$ is subdominant and can be neglected.

Placing an absorption grating into the image plane, the superposition of unperturbed intensity fringes of the phase grating and of the periodic intensity transmission function of the absorption grating, $A(\mathbf{r}) = \sum_l A_l \exp(i\mathbf{g}_l\mathbf{r})$, creates a characteristic Moiré fringe pattern, which then can be recorded in the detector plane. This Moiré fringe pattern again becomes distorted if the specimen is introduced into the beam path. For sufficiently large pixel size, the perturbed Moiré fringe pattern (integrated over the grating periods) can be approximated as [14]

$$J(\mathbf{r}) \approx \sum_{m,l} I_{-l}A_l \exp\left(i\mathbf{h}_m\Delta\tilde{\mathbf{r}}_\parallel\right) = \sum_{m,l} I_{-l}A_l \exp\left(i\mathbf{h}_m \, \tilde{w}/K\nabla_\parallel p'_{\varphi,\theta}(\mathbf{r}_\parallel)\right), \quad (9)$$

and is later used for solving the inverse problem to reconstruct the object contrast functions.

Inverse problem

The reconstruction procedure for grating-based laminography is the following: (a) retrieval of 2-D absorption, differential phase, and dark-field contrast maps from the stepping scans of the Moiré fringe pattern, go into (b) reconstruction of the 3-D laminographic object functions for the specimen's region of interest, and (c) stitching the ROIs to a full macroscopic 3-D image with microscopic resolution.

The inverse problem of the Talbot grating interferometer can be solved via a phase-stepping technique, where several interferograms with a different constant phase shift added to the reference interferometry pattern are recorded. Taking into account only the first diffraction orders ($l = \pm 1$), well-known rules of ordinary two-beam interferometry can be applied. For 1-D gratings the phase-stepping technique is realised via displacing one of the gratings in the direction parallel to $\mathbf{e}_u$. The differential phase map (the gradient of the x-ray phase transform) may directly be determined from a summation over each of the N interferograms of displacement $2\pi n/N$ weighted by $\exp(-2\pi in/N)$, where $n = 0, 1, 2, ..., N-1$., by (see for example [14])

$$\triangle\mathbf{h}\,\tilde{w}/K\nabla_\parallel p'_{\varphi,\theta}(\mathbf{r}_\parallel) \approx \arg\left\{\sum_{n=1}^{N} J_n(u,v,w') \exp\left(-2\pi in/N\right)\right\}. \quad (10)$$

Analysing the series of the interferograms $\sum_{n=1}^{N} \tilde{J}_n(u,v,w') \exp(-2\pi i n/N)\}$ for each pixel via Fourier analysis, the x-ray transforms of the object absorption function $\mu(\mathbf{r})$ can be retrieved together with the differential phase. One may also obtain the x-ray transforms of the effective scattering power $f(\mathbf{r})$, which results from the superposition of coherent Fresnel diffraction and mesoscale diffuse scattering of the specimen (see for example [17]).

The estimate of the unknown object functions $\rho(\mathbf{r})$ (which could be the linear attenuation coefficients $\mu(\mathbf{r})$, the real part of the refraction index $\tilde{\delta}(\mathbf{r})$, or the effective scattering power $f(\mathbf{r})$) from a series of projections reconstructed via Eq. (10) from the measured phase-stepping scans under constant θ but different rotation angles φ is performed by using the Fourier slice theorem. For the laminography case, the 2-D Fourier transforms $\mathscr{P}_{\varphi,\theta}(k_u,k_v)$ of the projections $p_{\varphi,\theta}(u,v)$ correspond to the cross-sections of the 3-D Fourier transform $\mathscr{M}(k_x,k_y,k_z)$ of the object functions $\rho(\mathbf{r})$ through the reciprocal image plane $(\mathbf{e}_u \times \mathbf{e}_v) \cdot \mathbf{k} = 0$, that is

$$\mathscr{P}(k_u,k_v) = \mathscr{M}(k_u \cdot \mathbf{e}_u + k_v \cdot \mathbf{e}_v) . \tag{11}$$

Since in the case of laminography in reciprocal space the 2-D Fourier transforms of the projections are inclined with respect to the $\mathbf{k}_z$ direction by the laminographic angle θ, the set of unbounded projections for different rotation angles does fill (and even oversamples) the region outside a double cone with the opening angle π-2θ, while the cone internal regions remain empty (non-sampled frequencies) [11]. As a consequence, laminographic reconstruction is an ill-posed inverse problem. The reconstruction process may provide only approximate object functions, the reconstruction of the accurate object function is impossible.

However, even full tomographic scans for such type of laterally extended samples cannot acquire the complete frequency domain, and, besides of representing also ill-posed inverse problem, additionally suffer from strongly angle-dependent transmission values [18].

The analytical reconstruction of the object functions $\rho(\mathbf{r})$ from its x-ray transforms can be performed by generating a so-called *compound image g* via back-projection and by the latter convolution with an *inverse filter function* $\hat{h}$ [11]. The inverse filter function $\hat{h}$ depends on the 3-D point spread function which is determined by the experimental geometry.

Here the relation between the compound image and projection is described by

$$\int_0^{2\pi} g_{\varphi,\theta}(x,y,z) \, d\varphi = \int_0^{2\pi} p_{\varphi,\theta}\left(T_{x,z}^{[1,3]}(\theta,\varphi) \cdot (x,y,z)^T\right) d\varphi , \tag{12}$$

with the laminographic transformation matrix

$$T_{x,z}(\theta,\varphi) = R_x(\theta - \pi/2) \cdot R_z(-\varphi) = \begin{bmatrix} \cos\varphi & -\sin\varphi & 0 \\ \sin\theta \cdot \sin\varphi & \sin\theta \cdot \cos\varphi & \cos\theta \\ \cos\theta \cdot \sin\varphi & \cos\theta \cdot \cos\varphi & -\sin\theta \end{bmatrix}, \tag{13}$$

and $T^{[1,3]}$ denotes a matrix where only the 1st and 3rd row of the matrix T is retained. Since

$$g(\mathbf{r}) = \{\rho \otimes h\}(\mathbf{r}) , \tag{14}$$

where $\otimes$ denotes a 3-D convolution, one obtains a *reconstruction equation*

$$\rho(\mathbf{r}) = \mathscr{F}_3^{-1}\{\mathscr{M}(\mathbf{k})\} = \mathscr{F}_3^{-1}\{[\mathscr{G} \cdot \bar{\mathscr{H}}](\mathbf{k})\} = \{g \otimes \bar{h}\}(\mathbf{r}) , \tag{15}$$

with $g = \mathscr{F}_3^{-1}\{\mathscr{G}\}$ and $\bar{h} = \mathscr{F}_3^{-1}\{\bar{\mathscr{H}}\} = \mathscr{F}_3^{-1}\{1/\mathscr{H}\}$.

Two reconstruction approaches can be employed for the laminography case: so-called filtering after backprojection and filtering before backprojection [19]. Filtering before backprojection has advantages concerning time and memory consumptions, and it is based on the relation

$$\{\mathscr{G}_{\varphi,\theta} \cdot \bar{\mathscr{H}}\}(\mathbf{k}) = \{\mathscr{P}_{\varphi,\theta} \cdot \bar{\mathscr{H}}_{\varphi,\theta}\}(T_{x,z}^{[1,3]}(\theta,\varphi) \cdot \mathbf{k}) \times \delta(T_{x,z}^{[2]}(\theta,\varphi) \cdot \mathbf{k}), \tag{16}$$

which holds when $\bar{\mathscr{H}}_{\varphi,\theta}$ is a 2-D section of the 3-D inverse filter function $\bar{\mathscr{H}}$ in the reciprocal space through a plane defined by a projection $\mathscr{P}_{\varphi,\theta}$ as

$$\bar{\mathscr{H}}_{\varphi,\theta}(k_u,k_v) = \bar{\mathscr{H}}(T^{-1}_{x,z}(\theta,\varphi)\cdot(k_u,0,k_v)^T). \tag{17}$$

According to the above statement, the 3-D convolution in Eq. (15) can be substituted by 2-D convolutions of projections with the filter function. The filter function can be derived from the 3-D inverse filter, which is less time consuming and leading to

$$\mathscr{F}_2\{\bar{h}_{\varphi,\theta}\} = \bar{\mathscr{H}}_{\varphi,\theta}(k_u,k_v) = \frac{\sin\theta}{2}|k_u|\,. \tag{18}$$

Moreover, since the filter neither depends on the laminographic rotation angle ϕ nor the reciprocal vector component k_v, the projection filtering can be efficiently implemented by a series of 1-D fast Fourier transforms.

Let

$$\mathscr{Q}_{\varphi,\theta}(k_u,k_v) = \{\mathscr{P}_{\varphi,\theta}\cdot\bar{\mathscr{H}}_{\varphi,\theta}\}(k_u,k_v) \overset{\mathscr{F}_2}{\Longleftrightarrow} q_{\varphi,\theta}(u,v) = \{p_{\varphi,\theta}\otimes\bar{h}_{\varphi,\theta}\}(u,v) \tag{19}$$

be a *filtered projection*. Applying Eq. (17), reconstruction equation (15) can be rewritten in the following two forms

$$\rho(\mathbf{r}) = \mathscr{F}_3^{-1}\left\{\int_0^{2\pi}\underbrace{\mathscr{Q}_{\varphi,\theta}(T^{[1,3]}_{x,z}(\theta,\varphi)\cdot\mathbf{k})\,\delta(T^{[2]}_{x,z}(\theta,\varphi)\cdot\mathbf{k})}_{\mathscr{M}_{\varphi,\theta}(\mathbf{k})}d\varphi\right\} = \int_0^{2\pi}q_{\varphi,\theta}(T^{[1,3]}_{x,z}(\theta,\varphi)\cdot\mathbf{r})\,d\varphi. \tag{20}$$

The above equation offers two fundamental ways to implement a reconstruction procedure: the reconstruction can be performed in reciprocal or directly in real space. For reconstructions from our experiments we used the second approach.

It should be noted that Eq. (20) can be directly applied to the reconstruction of the object functions $\mu(\mathbf{r})$ and $f(\mathbf{r})$. The reconstruction of the refractive index map $\tilde{\delta}(\mathbf{r})$ from the phase gradient projections requires an adaption of the filter function (Eq. (18)) to

$$\mathscr{F}_2\{\bar{h}_{\varphi,\theta}\} = \bar{\mathscr{H}}_{\varphi,\theta}(k_u,k_v) = \frac{\sin\theta}{2}\frac{1}{2\pi i}sgn(k_u) \tag{21}$$

corresponding to the Hilbert transform in real space [20].

Applying the reconstruction procedure to the recorded projections, absorption, phase and dark-field 3-D volumes were recontructed from the same experimental data set. The details on the instrumentation, imaging procedure and experimental conditions are described below.

3. Instrumentation and experiments

We have integrated both methods and performed our experiments at the laminography instrument of the ESRF ID19 beamline. The instrument has been developed by ANKA at Karlsruhe Institute of Technology (KIT). The set-up consists of the three main manipulation system units: laminography sample stage, detector manipulator, and the integrated Talbot grating interferometer.

The sample manipulation unit is designed to perform measurements in both tomography and laminography geometries. In the set-up at ID19 the laminography angle can be easily adjusted in the range from 45° to 70°. The detector manipulator holds a pixel array x-ray detector of requested resolution down to $0.5\,\mu$m pixel size. It also permits detector translation along the
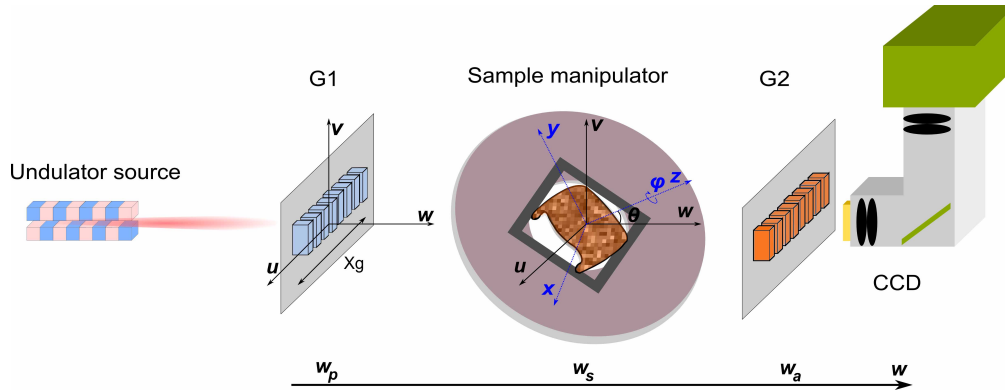
Fig. 2. Schematic view of the experimental set-up. The coordinate systems are the same as in the previous chapter, X_g denotes grating translation for the phase-stepping technique.

optical axis to set the wavefield propagation distances between the object and the detector plane (up to max. 1 m downstream of the sample rotation center).

The phase grating, in principle, can be mounted up- or downstream of the object plane. For the experiments reported here, we implemented a compact grating interferometer set-up with phase and absorption gratings downstream of the sample. The grating interferometry set-up was suspended above the sample manipulator from a frame-bridge system with two translation stages for the positioning of the gratings into the beam path and with a rotational stage for grating alignment (Fig. 2). The grating interferometer was further equiped with a piezo actuator in order to perform the phase-stepping. The system allows one to adjust any required Talbot distances in the range from 2 cm to 40 cm. In our experiments we employed a one-dimensional grating set-up. However, 2-D grating interferometers [21] will also work with this instrumentation.

The principal advantage of the laminography set-up at ID19 is a dedicated large-diameter sample rotation table with a large aperture for x-rays. When laminography measurements are performed, the rotational table is tilted versus the optical axis, so that the x-ray beam passes through the center of the rotation table, where the large aperture gives the x-rays travelling through the specimen without hitting the table itself or any specimen holder which could introduce an additional disturbance of the wavefield. Moreover, external positioning systems perform sample translation for 2-D scanning over an area up to 158 x158 mm². As a result, employing the laminographic rotation geometry, 3-D measurements of selected regions of interest (ROI) can be recorded with variable resolution, without special preparation (sample extraction). For example, the set-up allows first to measure low-resolution (preliminary) scans. After reconstruction, one is able to identify the most interesting ROIs and finally to zoom into these regions for high-resolution measurements. Also, continuous high-resolution screening of large specimen areas can be performed by repeating full-field computed laminography and systematically translating the sample through the center of the rotation table. In this way, combining the inherent full-field method with translational scanning, an enlarged effective field of view can be realized without drawbacks of additional artifacts.

For our measurements, temporal (longitudinal) coherence requirements of TGI-laminography have been satisfied by using the 1st harmonic of the ID19 undulator at ESRF with the peak energy at 18 keV and energy bandwidth dE/E of about 0.1. The ID19 source size and beamline length of 145 m guarantee more than sufficient spatial (transversal) coherence for the grating interferometer. The phase and absorption gratings with pitches of 2.4 μm were

fabricated by the LIGA process at KIT, the first made of $4\,\mu$m thick Ni (acting as a $\pi/2$-shift grating), the latter made of gold with a aspect ratio of 100. For the described experiments we have operated the TGI in the 5th Talbot order. The Moíre patterns were detected by use of the ESRF in-house developed CCD based "Frelon 2k" camera (with a 2048 x 2048 pixel array). By use of an optical lens coupled to a thin-film crystal scintillator (LuAg $125\,\mu$m), an effective pixel size of $5.02\,\mu$m was appropriately providing a field of view of about $10\,$mm x $10\,$mm. All datasets were acquired via phase-stepping scans with 4 steps per projection angle, and exposure time of $0.5\,$s per frame. The parchment specimens were visualized at a laminographic angle of 32 degrees; 1599 projections over 360 degrees rotation angle interval were acquired.

4. Results

In our work, the potential of laminography based on Talbot interferometry is demonstrated by a parchment study. For very long time, parchment has been used as a material for writing. A group of antique collective texts from the Hebrew Bible, para-biblical and Jewish sectarian texts, was made by parchment from the animal skin, such as sheep and goats [22] is known as the Dead Sea Scrolls. Due to the storage conditions, exposure to light, as well as influence of humidity and bacteria the persistence of these manuscripts is in great danger. In order to preserve such significant historical documents of mankind, understanding of parchment structure and its deterioration processes is of fundamental interest for our cultural heritage.

Parchment degradation has been studied by other x-ray methods such as x-ray diffraction and fluorescence analysis, and x-ray absorption near edge structure [23, 24]. Recently, absorption tomography of a small piece of the Dead Sea Scrolls indicated the advantages of 3-D non-destructive imaging [25].

In order to understand how the degradation of the parchment occurs we examine freshly prepared parchment in comparison to already degradated parchment from the Dead Sea Scrolls. Due to inhomogeneity of parchment and its complex structure, we applied Talbot interferometry based laminography so that multiple-contrast information can be used.

The preparation techniques of parchment and ink from Dead Sea Scrolls have been studied via several analytical techniques, which should allow mimicking the traditions used by the ancient Jewis scribes, who prepared their own parchment and ink for the Dead Sea Scrolls. Scientists are interested to find out, whether their mimicked parchment fabrication process goes back in history to the recipes which were used at Qumran and other sites during the second Temple period (300 BC-70 AD).

There are two main recipes today used by orthodox circles in Jerusalem: One based on the slake (lye) method, whereas the second one uses potash made of ashes of burned wood. Both, however, start with the depilation, or de-hairing, of the fresh hide after fat and tissue have been removed, either mechanically or manually, by continuous scraping and grinding the hide to the wanted thickness. After depilation, the raw hide is tanned in a concoction made of organic matter such as Rhus leaves or oak galls known for their tanning properties. Subsequently, the hide is rinsed well and is stretched over a frame in a well-vented room without making use of sunlight that eventually would destroy the skin. When the entire skin is dry, which can take one or two days depending on the temperature, it is cut into pages of specific size. The fresh parchment skin we used in this study was prepared according to the slake/lye technique.

Here we apply laminography within a feasibility study, investigating whether we can get structural information from both fresh and historical parchment. In more detail, according to fabrication procedure and the type of material used, we expect morphological variation going from the bottom to the top side of the parchment.

Slices through the reconstructed 3-D volumes of absorption, dark-field and phase contrast from the freshly prepared parchment are shown in Fig. 3(a-c), respectively. The slices corre-
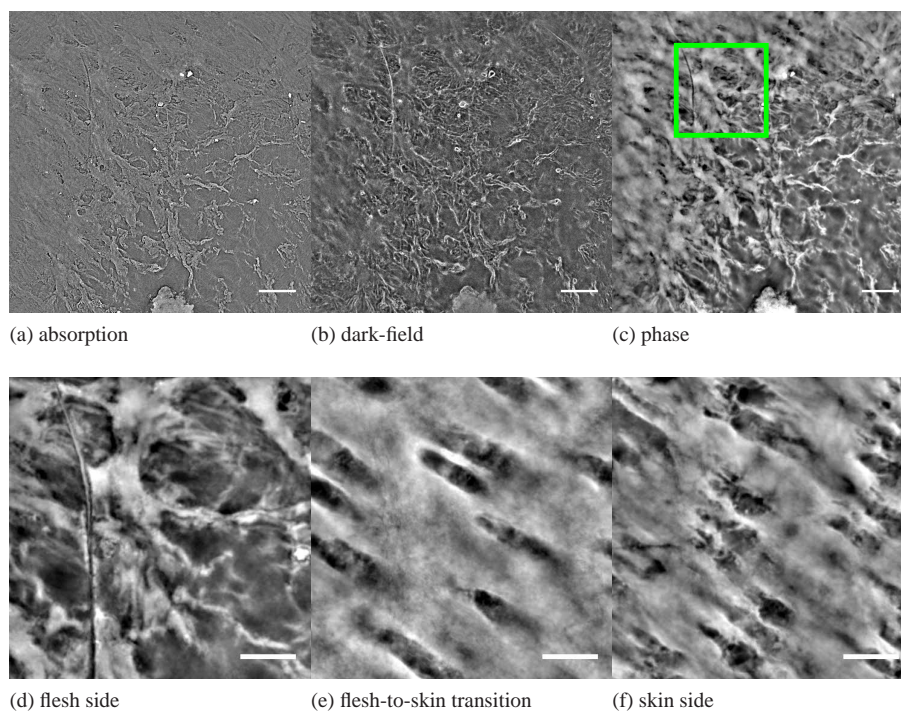
Fig. 3. Figures (a-c) shows absorption, dark-field and phase contrast slices through the reconstructed 3-D volume of the freshly prepared parchment. The scale bar is 1 mm. Figures (d-f) are the phase contrast slices at the different height, through the 3-D laminographic volume of the parchment, the thickness of the piece is 280 μm. Figures (d) and (f) are recto (skin) and verso (flesh) sides correspondingly. Figure (e) depicts a slice through the middle of the volume at 140 μm from the surface. All images are the zoomed ROI from the Fig. (c). The scale bar is 500 μm.

spond to the verso (back or flesh) side of the parchment. All three images of different contrast show details of the fat-like structure in the parchment. Further, the absorption contrast image (Fig. 3a) indicates highly absorbing particle-like components, which could come from the sample preparation or storage. The dark-field image (Fig. 3b) enhances interfaces inside the parchment structure and especially highlights the scattering signal from the particles within it. Parchment is a weakly absorbing material. As expected, the phase map (Fig. 3c) gives best contrast, at least, for the parchment tissue. The three slices selected in Fig. 3(d-f) zoom into a region of interest and show phase contrast images for three different but equidistant depths. In the slices we observe a characteristic variation of the porous microstructure, especially from Fig. 3d to 3e. The slices also indicate lateral density variation within the parchment material.

A piece of degradated parchment from one of the Dead Sea Scrolls (QUM 922, Cave 4) is visualized in Fig. 4(a-f). One can clearly observe the structural changes due to degradation if comparing the slices of fresh and historical specimen, already by naked eye, both are fundamentally different. Absorption, dark-field and phase contrast slices taken from the same depth of the parchment are shown in Fig. 4(a-c), demonstrating the strong structural changes suffered over time. The dark-field image 4(b) shows that the area density of the interfaces inside the parchment has considerably increased which might be due to the appearance of micro-fissures inside the former tissue. Overall, the parchment's structure has decomposed and shrunk to a
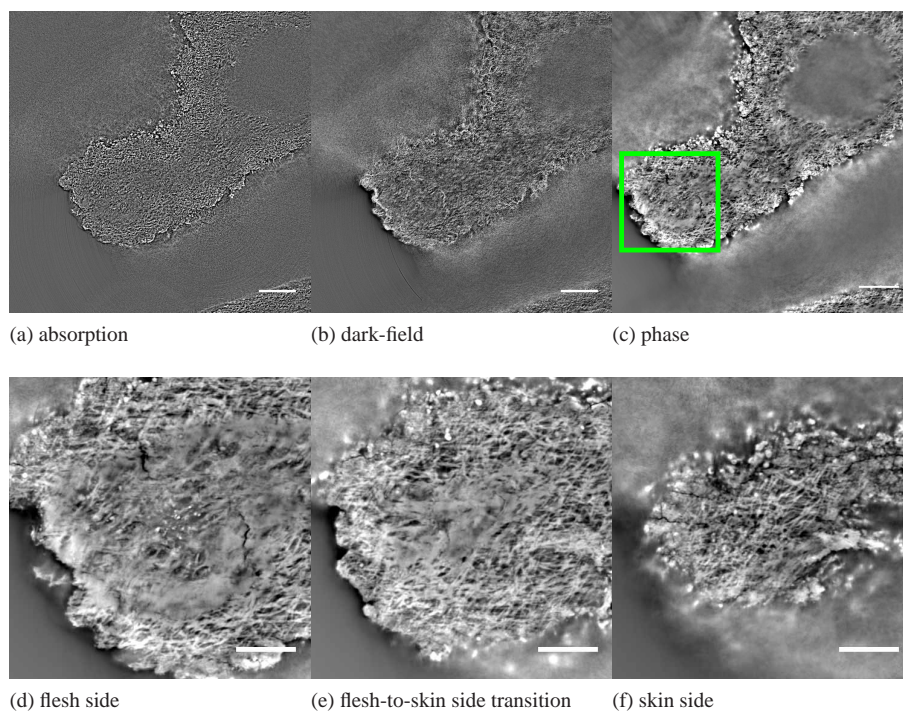
Fig. 4. Figures (a-c) show absorption, dark-field, and phase contrast slices through the reconstructed 3-D volume from the small piece of Dead Sea scrolls. The scale bar is 1 mm. As for the freshly prepared parchment, figures (d-f) show phase contrast slices at the different depth of parchment (zoomed region from (c)). The total thickness of the parchment from the Dead Sea scrolls is about 150 μm. The scale bar is 500 μm.

large extent. Also, significant warpage occured. On all phase contrast slices taken at different depth of the parchment, Fig. 4(d-f), we clearly discover the formation of collagen fibrils, particle-like structures and micro-cracks compared to the formerly much more homogeneous material of fresh parchment. The detailed morphology of collagen fibrils varies from one slice to the next. At the edges of parchment the collagen fibrils are more structured and more dense. So, in the examined sample the parchment was preserved better at the edges. The observation, that the collagen system seems to be more disordered in the center of parchment, supports the earlier hypothesis that the deterioration might have developed from the inside towards the outside [24].

Under methodical points of view, we may conclude on the principal feasibility of TGI-laminography as a very promising technique for systematic studies of historical parchment degradation, such as Dead Sea Scrolls and others. Moreover, applying the phase-stepping technique, images of different contrast modes can be retrieved making absorption, dark-field and phase contrast simultaneously available. Systematic use of multiple-contrast images will provide more complementary understanding of structural changes within a 3-D volume. Since the method enables us to non-destructively scan large volume of parchment and to zoom into various regions of interst with variably chosen resolution, the technique seems presently to be the only 3-D method allowing to perform representative studies of structure changes.

5. Conclusions

Laminography with integrated Talbot grating interferometry has been theoretically described and experimentally realized by implementing a dedicated instrumental set-up of ANKA/KIT at the ESRF ID19 Imaging Beamline. Summarizing the forward problem of image formation and the inverse problem for data retrieval of grating's-based laminography, the main reconstruction equations have been developed in both real and reciprocal space including a computation-time efficient 1-D projection filter and a filter adapted to retrieve the spatial electron density modulation of the object from differential phase images.

Talbot interferometric laminography combines the advantages of both methods: it simultaneously yields information on the 3-D distribution of the specimen's properties to attenuate, to scatter and to shift the phase of the probing x-ray wave field within a single measurement. It allows zooming into various selected regions of interest as well as scanning of large sample areas. Presently we are able to provide spatial resolutions in the order of 5 micrometres. This enables non-destructive 3-D screening of laterally extended devices and samples containing light-weight materials.

In the context of archeometry, we demonstrated the potential of this non-destructive technique by comparing the structure of freshly prepared parchment following historical recipes and already degraded historical parchment taken from the Dead Sea Scrolls, that are about 2000 years old.